

BSSN in Spherical Symmetry

J. David Brown

Department of Physics, North Carolina State University, Raleigh, NC 27695 USA

The BSSN (Baumgarte–Shapiro–Shibata–Nakamura) formulation of the Einstein evolution equations is written in spherical symmetry. These equations can be used to address a number of technical and conceptual issues in numerical relativity in the context of a single Schwarzschild black hole. One of the benefits of spherical symmetry is that the numerical grid points can be tracked on a Kruskal–Szekeres diagram. Boundary conditions suitable for puncture evolution of a Schwarzschild black hole are presented. Several results are shown for puncture evolution using a fourth–order finite difference implementation of the equations.

I. INTRODUCTION

The Baumgarte–Shapiro–Shibata–Nakamura [1, 2] formulation of the Einstein equations has been in widespread use in the numerical relativity community for a number of years. BSSN is the formulation used with the successful moving puncture technique for black hole simulations [3, 4]. Currently several groups are using BSSN with moving punctures to model the gravitational wave signal from binary black hole mergers. (See, for example, Refs. [5, 6, 7, 8, 9, 10, 11, 12].)

There are still many open issues in numerical relativity, both technical and conceptual. One would like to explore these issues in an efficient manner. Current three–dimensional codes can take days or longer on a multi–processor computer cluster to carry out each simulation. By assuming spherical symmetry we can reduce the run time to minutes on a single processor. Thus there is an enormous practical advantage in assuming spherical symmetry. Of course, with a spherically symmetric (one–dimensional) code we are limited to issues that can be addressed in the context of a single Schwarzschild black hole. Furthermore there is no guarantee that the results one finds in spherical symmetry will transfer to the three–dimensional setting—in three dimensions there is a much wider range of possible problems that can arise. On the other hand, if a particular idea cannot be applied successfully in one dimension, it is unlikely to work in three.

This article describes the one–dimensional code used in Refs. [13, 14, 15] to explore the evolution of Schwarzschild black holes. Such a code could also be used to examine various slicing and shift conditions, to explore different types of boundary conditions, and to experiment with constrained and unconstrained evolution schemes. Valuable insights into these and other problems can be gained with the help of a one–dimensional code.

Many questions that one can address with a one–dimensional code are independent of the formulation of the Einstein evolution equations. But it is reasonable to expect that the behavior of a one–dimensional code based on the BSSN formulation will be closer to existing three–dimensional BSSN codes. This is important when considering issues related to stability, constraint violations, *etc.* Also note that the Γ –driver shift condition, currently used for puncture evolution studies of binary

black hole coalescence, makes explicit use of the conformal connection functions Γ^a . The conformal connection functions are basic variables in the BSSN formulation.

There is a technical obstacle to writing the BSSN formulation of Einstein’s equations in spherical symmetry. More generally, there is a technical obstacle to writing BSSN in spherical coordinates. The obstacle is this: The BSSN equations assume that the conformal metric has determinant equal to one. This condition is not generally covariant. In practice this is a problem because we typically use initial data that is conformally flat, and we naturally choose the initial conformal metric to be flat. But in spherical coordinates the flat metric does not have unit determinant. This obstacle can be overcome by generalizing the BSSN equations to allow for a conformal metric with non–unit determinant. The way to do so was presented in Ref. [16], and is reviewed in Sec. 2.

The generalized BSSN equations (GBSSN) are invariant under conformal transformations [16]. This invariance is broken when one chooses an evolution equation for the determinant of the conformal metric. There are two natural choices that yield the “Lagrangian case” and the “Eulerian case”. In Sec. 3 I show how the GBSSN equations are reduced to spherical symmetry for each of these cases. The level of hyperbolicity for these equations is discussed in Sec. 4.

In this work I focus on puncture evolution for a Schwarzschild black hole. The puncture is located at the coordinate origin. In spherical coordinates, the origin is also a coordinate singularity. Clearly the boundary conditions at the origin play an important role. In Sec. 5 I describe sets of boundary conditions that work well in practice. In Sec. 6 I show how the numerical grid points can be mapped to a Kruskal diagram. This allows us to visualize the spacelike slice as it evolves, and track the distribution of grid points relative to the horizon and physical singularity. Section 7 presents some results for puncture evolution in one dimension. These results use the standard “1+log” slicing condition

$$\partial_t \alpha = \beta^a \partial_a \alpha - 2\alpha K, \quad (1)$$

or the related condition obtained by dropping the advection term $\beta^a \partial_a \alpha$. Here, α is the lapse function, β^a is the shift vector, and K is the trace of the extrinsic

curvature. For the shift vector, the examples use either vanishing shift or the Γ -driver condition

$$\partial_t \beta^a = \frac{3}{4} B^a + \beta^c \partial_c \beta^a, \quad (2a)$$

$$\partial_t B^a = \partial_t \Gamma^a + \beta^c \partial_c B^a - \beta^c \partial_c \Gamma^a - \eta B^a. \quad (2b)$$

Variants of the Γ -driver condition are obtained by dropping one or more of the advection terms $\beta^c \partial_c \beta^a$, $\beta^c \partial_c B^a$, or $\beta^c \partial_c \Gamma^a$ [7, 17].

II. GENERALIZED BSSN EQUATIONS

The BSSN equations can be generalized to allow for the possibility that the determinant of the conformal metric differs from unity [16]. The conformal metric g_{ab} and the trace-free part of the extrinsic curvature A_{ab} are defined by

$$\bar{g}_{ab} = e^{4\phi} g_{ab}, \quad (3a)$$

$$K_{ab} = e^{4\phi} \left(A_{ab} + \frac{1}{3} g_{ab} K \right), \quad (3b)$$

where \bar{g}_{ab} and K_{ab} are the physical spatial metric and extrinsic curvature. The variable ϕ is the conformal factor and $K \equiv \bar{g}^{ab} K_{ab}$ is the trace of the physical extrinsic curvature. The conformal connection functions are defined by

$$\Gamma^a \equiv g^{bc} \Gamma_{bc}^a = -\frac{1}{\sqrt{g}} \partial_b (\sqrt{g} g^{ab}), \quad (4)$$

where Γ_{bc}^a are the Christoffel symbols built from the conformal metric. The evolution equation for Γ^a is obtained by differentiating this definition and using the momentum constraint. The BSSN variables are ϕ , g_{ab} , A_{ab} , K , and Γ^a .

In vacuum, the generalized BSSN evolution equations (the GBSSN equations) are¹

$$\partial_\perp \phi = -\frac{1}{12} \partial_\perp \ln g - \frac{1}{6} \alpha K, \quad (5a)$$

$$\partial_\perp g_{ab} = \frac{1}{3} g_{ab} \partial_\perp \ln g - 2\alpha A_{ab}, \quad (5b)$$

$$\begin{aligned} \partial_\perp A_{ab} &= \frac{1}{3} A_{ab} \partial_\perp \ln g - 2\alpha A_{ac} A_b^c + \alpha A_{ab} K \\ &+ e^{-4\phi} [\alpha \bar{R}_{ab} - \bar{D}_a \bar{D}_b \alpha]^{\text{TF}}, \end{aligned} \quad (5c)$$

$$\partial_\perp K = \frac{1}{3} \alpha K^2 + \alpha A_{ab} A^{ab} - \bar{D}^a \bar{D}_a \alpha, \quad (5d)$$

$$\begin{aligned} \partial_\perp \Gamma^a &= -\frac{1}{3} \Gamma^a \partial_\perp \ln g - \frac{1}{6} g^{ab} \partial_b \partial_\perp \ln g - 2A^{ab} \partial_b \alpha \\ &+ 2\alpha \left[\Gamma_{bc}^a A^{bc} + 6A^{ab} \partial_b \phi - \frac{2}{3} g^{ab} \partial_b K \right], \end{aligned} \quad (5e)$$

where \bar{R}_{ab} is the physical Ricci tensor, \bar{D}_a is the physical covariant derivative, and D_a is the conformal covariant derivative. The shift vector β^a is buried in the time derivative operator, $\partial_\perp \equiv \partial_t - \mathcal{L}_\beta$. Also note that TF stands for the trace-free part of the expression in brackets.

The variables ϕ , g_{ab} , A_{ab} , and K are defined as tensors with no density weights. The transformation rules for the conformal connection functions Γ^a are determined by the transformation rules for the Christoffel symbols Γ_{bc}^a and the definition Eq. (4). The GBSSN equations do not assume $g = 1$, and we are free to choose how g evolves in time. Two natural choices are the ‘‘Eulerian condition’’ $\partial_\perp \ln g = 0$ and the ‘‘Lagrangian condition’’ $\partial(\ln g)/\partial t = 0$, which implies $\partial_\perp \ln g = -2D_a \beta^a$.

In the traditional BSSN formulation, the restriction $g = 1$ appears as an extra constraint. In most numerical codes this constraint is enforced by replacing g_{ab} with $g_{ab}/g^{1/3}$ at the end of each time step. There is no clear equivalence between the traditional BSSN formulation and GBSSN with either the Eulerian (GBSSN-E) or Lagrangian (GBSSN-L) conditions. In particular, observe that there are 16 field variables evolved by the GBSSN equations (namely ϕ , the six components of g_{ab} , the five components of A_{ab} , K , and the three components of Γ^a) but only 15 variables in the traditional BSSN system. One consequence of this difference is a mismatch in the number of characteristic fields for GBSSN and traditional BSSN. In spite of this difference one might guess that GBSSN with the Lagrangian condition $\partial g/\partial t = 0$ is closely related to traditional BSSN. With GBSSN-L the determinant g , which can be set to 1 by initial conditions, remains constant throughout the evolution. Indeed, a qualitative comparison between the results presented in Section VII and results obtained in three dimensions with traditional BSSN shows that GBSSN-L and traditional BSSN yield very similar behavior for puncture evolution of a single Schwarzschild black hole. For example, compare Figs. 7–10 of this paper with Fig. 1 of Ref. [7].

Although GBSSN-L and traditional BSSN are similar in some respects, GBSSN-L contains an extra characteristic field. That field travels along the integral curves of the time flow vector field ∂_t . Thus, this field has a characteristic speed that, when measured with respect to observers at rest in the spacelike hypersurfaces, depends on the shift vector. This is not necessarily bad, but it is at least unusual and unphysical. For a typical formulation of the Einstein equations, the characteristic speeds are independent of the shift vector as long as any dynamical gauge conditions are expressed in terms of the normal derivative operator $\partial_\perp = \partial_t - \mathcal{L}_\beta$. GBSSN-L breaks this pattern. On the other hand, for GBSSN-E, the extra characteristic is a zero-speed mode. As a result, the Eulerian condition yields a more simple and in some sense more physical version of the GBSSN system.

Finally, note that the variable ϕ can be replaced with a new variable $\chi \equiv e^{-4\phi}$. It is straightforward to rewrite the GBSSN equations in terms of χ . Note that χ , like

¹ Equation (5c) corrects a sign error in Ref. [16].

ϕ , is a scalar with no density weight. The variable ϕ was used in Ref. [4], while the authors of Ref. [3] used χ . Reference [7] includes comparisons between the two choices for black hole puncture evolution.

III. GBSSN REDUCED BY SPHERICAL SYMMETRY

Let the spatial coordinates be denoted by r , θ , and φ . The GBSSN equations are reduced to spherical symmetry with the following ansatz for the metric:

$$g_{ab} = \begin{pmatrix} g_{rr} & 0 & 0 \\ 0 & g_{\theta\theta} & 0 \\ 0 & 0 & g_{\theta\theta} \sin^2 \theta \end{pmatrix} \quad (6)$$

The ansatz for the trace-free part of the extrinsic curvature is

$$A_{ab} = A_{rr} \begin{pmatrix} 1 & 0 & 0 \\ 0 & -g_{\theta\theta}/(2g_{rr}) & 0 \\ 0 & 0 & -g_{\theta\theta} \sin^2 \theta / (2g_{rr}) \end{pmatrix} \quad (7)$$

and for the conformal connection functions,

$$\Gamma^a = \begin{pmatrix} \Gamma^r \\ -\cos \theta / (g_{\theta\theta} \sin \theta) \\ 0 \end{pmatrix} \quad (8)$$

The dynamical variables are now ϕ or χ , g_{rr} , $g_{\theta\theta}$, A_{rr} , K , and Γ^r . They are all functions of the spatial coordinate r and time t .

For the rest of this paper I will use the variable χ rather than ϕ . I also use $\partial_{\perp} \ln g = -2v D_a \beta^a$ where $v = 0$ gives the Eulerian condition and $v = 1$ gives the Lagrangian condition. In spherical symmetry, the GBSSN equations are as follows:

$$\partial_t \chi = \frac{2K\alpha\chi}{3} - \frac{v\beta^r g_{rr}' \chi}{3g_{rr}} - \frac{2v\beta^r g_{\theta\theta}' \chi}{3g_{\theta\theta}} - \frac{2}{3} v \beta^{r'} \chi + \beta^r \chi', \quad (9a)$$

$$\partial_t g_{rr} = -2A_{rr}\alpha - \frac{1}{3} v \beta^r g_{rr}' + \beta^r g_{rr}' - \frac{2g_{rr} v \beta^r g_{\theta\theta}'}{3g_{\theta\theta}} + 2g_{rr} \beta^{r'} - \frac{2}{3} g_{rr} v \beta^{r'}, \quad (9b)$$

$$\partial_t g_{\theta\theta} = \frac{A_{rr} g_{\theta\theta} \alpha}{g_{rr}} - \frac{g_{\theta\theta} v \beta^r g_{rr}'}{3g_{rr}} - \frac{2}{3} v \beta^r g_{\theta\theta}' + \beta^r g_{\theta\theta}' - \frac{2}{3} g_{\theta\theta} v \beta^{r'}, \quad (9c)$$

$$\begin{aligned} \partial_t A_{rr} = & -\frac{2\alpha A_{rr}^2}{g_{rr}} + K\alpha A_{rr} - \frac{v\beta^r g_{rr}' A_{rr}}{3g_{rr}} - \frac{2v\beta^r g_{\theta\theta}' A_{rr}}{3g_{\theta\theta}} - \frac{2}{3} v \beta^{r'} A_{rr} + 2\beta^{r'} A_{rr} + \frac{2\alpha\chi (g_{rr}')^2}{3g_{rr}^2} \\ & - \frac{\alpha\chi (g_{\theta\theta}')^2}{3g_{\theta\theta}^2} - \frac{\alpha(\chi')^2}{6\chi} - \frac{2g_{rr}\alpha\chi}{3g_{\theta\theta}} + \beta^r A_{rr}' + \frac{2}{3} g_{rr}\alpha\chi\Gamma^{r'} - \frac{\alpha\chi g_{rr}' g_{\theta\theta}'}{2g_{rr}g_{\theta\theta}} + \frac{\chi g_{rr}' \alpha'}{3g_{rr}} \\ & + \frac{\chi g_{\theta\theta}' \alpha'}{3g_{\theta\theta}} - \frac{\alpha g_{rr}' \chi'}{6g_{rr}} - \frac{\alpha g_{\theta\theta}' \chi'}{6g_{\theta\theta}} - \frac{2\alpha' \chi'}{3} - \frac{\alpha\chi g_{rr}''}{3g_{rr}} + \frac{\alpha\chi g_{\theta\theta}''}{3g_{\theta\theta}} - \frac{2\chi\alpha''}{3} + \frac{\alpha\chi''}{3}, \end{aligned} \quad (9d)$$

$$\partial_t K = \frac{3\alpha A_{rr}^2}{2g_{rr}^2} + \frac{K^2\alpha}{3} + \beta^r K' + \frac{\chi g_{rr}' \alpha'}{2g_{rr}^2} - \frac{\chi g_{\theta\theta}' \alpha'}{g_{rr}g_{\theta\theta}} + \frac{\alpha' \chi'}{2g_{rr}} - \frac{\chi\alpha''}{g_{rr}}, \quad (9e)$$

$$\begin{aligned} \partial_t \Gamma^r = & -\frac{v\beta^r (g_{\theta\theta}')^2}{g_{rr}g_{\theta\theta}^2} + \frac{A_{rr}\alpha g_{\theta\theta}'}{g_{rr}^2 g_{\theta\theta}} - \frac{v\beta^{r'} g_{\theta\theta}'}{3g_{rr}g_{\theta\theta}} + \frac{\beta^{r'} g_{\theta\theta}'}{g_{rr}g_{\theta\theta}} + \beta^r \Gamma^{r'} + \frac{A_{rr}\alpha g_{rr}'}{g_{rr}^3} - \frac{4\alpha K'}{3g_{rr}} - \frac{2A_{rr}\alpha'}{g_{rr}^2} \\ & + \frac{v g_{rr}' \beta^{r'}}{2g_{rr}^2} - \frac{g_{rr}' \beta^{r'}}{2g_{rr}^2} - \frac{3A_{rr}\alpha\chi'}{g_{rr}^2 \chi} + \frac{v\beta^r g_{rr}''}{6g_{rr}^2} + \frac{v\beta^r g_{\theta\theta}''}{3g_{rr}g_{\theta\theta}} + \frac{v\beta^{r''}}{3g_{rr}} + \frac{\beta^{r''}}{g_{rr}}, \end{aligned} \quad (9f)$$

Primes denote derivatives with respect to r . Note that I am following the common practice of using Γ^r on the right-hand side only if it appears differentiated.

The Hamiltonian constraint is defined by $\mathcal{H} \equiv K^2 - K_{ab}K^{ab} + \bar{R}$ and the momentum constraint is defined by $\mathcal{M}_a \equiv \bar{D}_b K_a^b - \bar{D}_a K$. (Indices on K_{ab} are raised with the physical metric.) With BSSN we also have constraints that arise from the definition of the conformal connection functions: $\mathcal{G}^a \equiv \Gamma^a - g^{bc}\Gamma_{bc}^a$. In spherical symmetry these

constraints become

$$\mathcal{H} = -\frac{3A_{rr}^2}{2g_{rr}^2} + \frac{2K^2}{3} - \frac{5\chi'^2}{2\chi g_{rr}} + \frac{2\chi''}{g_{rr}} + \frac{2\chi}{g_{\theta\theta}} - \frac{2\chi g_{\theta\theta}''}{g_{rr}g_{\theta\theta}} + \frac{2\chi'g_{\theta\theta}'}{g_{rr}g_{\theta\theta}} + \frac{\chi g_{rr}'g_{\theta\theta}'}{g_{rr}^2g_{\theta\theta}} - \frac{\chi'g_{rr}'}{g_{rr}^2} + \frac{\chi g_{\theta\theta}'^2}{2g_{rr}g_{\theta\theta}^2}, \quad (10a)$$

$$\mathcal{M}_r = \frac{A_{rr}'}{g_{rr}} - \frac{2K'}{3} - \frac{3A_{rr}\chi'}{2\chi g_{rr}} + \frac{3A_{rr}g_{\theta\theta}'}{2g_{rr}g_{\theta\theta}} - \frac{A_{rr}g_{rr}'}{g_{rr}^2}, \quad (10b)$$

$$\mathcal{G}^r = -\frac{g_{rr}'}{2g_{rr}^2} + \Gamma^r + \frac{g_{\theta\theta}'}{g_{rr}g_{\theta\theta}}, \quad (10c)$$

and the constraint evolution system is

$$\partial_t \mathcal{H} = \beta^r \mathcal{H}' + \frac{2}{3} \alpha K \mathcal{H} - \frac{2\alpha A_{rr} \chi \mathcal{G}^{r'}}{g_{rr}} - \frac{2\alpha \chi}{g_{rr}} \mathcal{M}_r' + \left[\frac{\alpha \chi'}{g_{rr}} + \frac{\alpha \chi g_{rr}'}{g_{rr}^2} - \frac{4\alpha' \chi}{g_{rr}} - \frac{2\alpha \chi g_{\theta\theta}'}{g_{rr}g_{\theta\theta}} \right] \mathcal{M}_r, \quad (11a)$$

$$\partial_t \mathcal{M}_r = \beta^r \mathcal{M}_r' + \beta^{r'} \mathcal{M}_r + \alpha K \mathcal{M}_r - \frac{\alpha'}{3} \mathcal{H} + \frac{\alpha}{6} \mathcal{H}' + \frac{2}{3} \alpha \chi \mathcal{G}^{r''} + \left[\frac{2\alpha' \chi}{3} - \frac{\alpha \chi'}{3} + \frac{\alpha \chi g_{\theta\theta}'}{g_{\theta\theta}} \right] \mathcal{G}^{r'}, \quad (11b)$$

$$\partial_t \mathcal{G}^r = \beta^r \mathcal{G}^{r'} + \frac{2\alpha}{g_{rr}} \mathcal{M}_r. \quad (11c)$$

In the three-dimensional application of BSSN one must face the possibility that under numerical evolution A_{ab} will not remain trace-free. In most three-dimensional codes the components A_{ab} are adjusted at the end of each timestep to maintain the constraint $A_{ab}g^{ab} = 0$. In spherical symmetry A_{ab} is automatically traceless by virtue of the ansatz Eq. (7). As discussed previously, the determinant of the conformal metric is not constrained in the generalized BSSN formulation.

IV. HYPERBOLICITY

Consider the Eulerian ($\partial_{\perp} g = 0$) and Lagrangian ($\partial_{\perp} g = -2D_a \beta^a$) formulations with 1+log slicing Eq. (1) and either Γ -driver shift or vanishing shift. With the 1+log slicing and Γ -driver shift conditions we can either include or exclude the advection terms. These cases will be labeled E for Eulerian and L for Lagrangian. A superscript $+$ or $-$ will denote the inclusion or exclusion of the advection term in the 1+log slicing condition. A subscript $+$ or $-$ will denote the inclusion or exclusion of all advection terms in the Γ -driver shift condition. For example, E_{\pm}^+ represents the Eulerian case with 1+log slicing that includes the advection term and Γ -driver shift that includes all advection terms. Similarly, L_{\pm}^+ denotes the Lagrangian case with 1+log slicing that includes the advection term and Γ -driver shift that excludes all advection terms. I also use a subscript 0 to denote vanishing shift. In these cases the advection term in the 1+log slicing condition vanishes, so the superscript can be omitted. Thus, E_0 and L_0 refer to the Eulerian and Lagrangian cases with vanishing shift.

The results on hyperbolicity reported here were obtained using pseudo-differential techniques [18, 19]. These techniques apply to systems of PDE's that have first order time derivatives and second order space deriva-

tives. Pseudo-differential methods can only distinguish between weak and strong hyperbolicity; other methods must be used to check for symmetric hyperbolicity.

For the cases E_0 , L_0 , which have vanishing shift, the full system (equations of motion and 1+log slicing) is strongly hyperbolic. For the cases with nonvanishing shift, the full system (equations of motion plus gauge conditions) is strongly hyperbolic as long as certain inequalities among the field variables are satisfied.

There are three characteristic fields that are common to all cases. These are:

$$\Gamma^r \mp \frac{3}{2\sqrt{g_{rr}^3 \chi}} A_{rr} + \frac{1}{2g_{rr} \chi} \chi' - \frac{1}{2g_{rr}^2} g_{rr}' + \frac{1}{2g_{rr} g_{\theta\theta}} g_{\theta\theta}' \pm \frac{1}{\sqrt{g_{rr} \chi}} K, \quad (12a)$$

$$\Gamma^r + \frac{2}{\chi g_{rr}} \chi' - \frac{1}{2g_{rr}^2} g_{rr}' - \frac{1}{g_{rr} g_{\theta\theta}} g_{\theta\theta}'. \quad (12b)$$

The fields (12a) have proper speeds ± 1 as measured by observers at rest in the spacelike slices. The field (12b) has vanishing speed. All cases in which the advection term is included in the 1+log slicing condition (or the shift vanishes) have characteristic fields

$$\alpha' \pm \sqrt{2\alpha g_{rr} / \chi} K \quad (13)$$

with proper speeds $\pm \sqrt{2/\alpha}$.

The remaining characteristic fields and speeds depend on the details of the formulation and the gauge conditions. For E_0 there are two characteristic fields in addition to those displayed in Eqs. (12), (13). Both are zero speed modes. For L_0 , the remaining characteristic fields have speeds 0 and $\hat{\beta}^r$, where $\hat{\beta}^r \equiv \sqrt{g_{rr}/\chi} \beta^r / \alpha$ is the proper length shift per unit proper time.

For the cases E_{\pm}^+ and L_{\pm}^+ there are four characteristic fields in addition to those displayed above. For

E_{\pm}^{+} the extra characteristic fields have speeds 0, 0, $\pm\sqrt{3/(\alpha^2\chi)}/2$. This system is strongly hyperbolic as long as $8\alpha\chi \neq 3$. For L_{\pm}^{+} , the remaining characteristic fields have speeds 0, $\hat{\beta}^r$, $\pm\sqrt{1/(\alpha^2\chi)}$ and the requirements for strong hyperbolicity are $\sqrt{g_{rr}}|\beta^r| \neq 1$ and $2\alpha\chi \neq 1$. For the case E_{\pm}^{-} , the remaining characteristic fields have speeds 0, $\hat{\beta}^r$, $[\hat{\beta}^r \pm \sqrt{(\hat{\beta}^r)^2 + 3/(\alpha^2\chi)}]/2$ and the requirement for strong hyperbolicity is $(8\alpha\chi - 3) \neq \pm 4\sqrt{2\alpha\chi g_{rr}}\beta^r$. For the case L_{\pm}^{-} , the remaining characteristic fields have speeds $\hat{\beta}^r$, $\hat{\beta}^r$, $[\hat{\beta}^r \pm \sqrt{(\hat{\beta}^r)^2 + 4/(\alpha^2\chi)}]/2$ and the requirement for strong hyperbolicity is $2\alpha\chi - 1 \neq \pm\sqrt{2\alpha\chi g_{rr}}\beta^r$. In all cases, strong hyperbolicity can be spoiled if one or more of the fields g_{rr} , $g_{\theta\theta}$, χ or α vanishes. I have not carried out a complete analysis of the restrictions on hyperbolicity for the cases E_{\pm}^{-} and L_{\pm}^{-} .

The restrictions on strong hyperbolicity are not a consequence of the reduction to spherical symmetry. Precisely the same restrictions are found for the full three-dimensional GBSSN systems. In three dimensions one analyzes hyperbolicity by choosing a unit normal covector n_a and projecting the principal parts of the equations of motion in directions normal and tangential to n_a . In this way the principal symbol splits into blocks that transform as scalars, vectors, and trace-free tensors under rotations about the normal direction. The vector and tensor blocks are strongly hyperbolic without restriction. The scalar block in three dimensions is identical to the principal symbol for the spherically symmetric GBSSN system. It follows that GBSSN has the same restrictions on strong hyperbolicity in three dimensions as it has in spherical symmetry.

It should be noted that for traditional BSSN with 1+log slicing and Γ -driver shift, including all advection terms, strong hyperbolicity requires $2\alpha\chi \neq 1$ [19]. For traditional BSSN with 1+log slicing and Γ -driver shift and various combinations of advection terms, the restrictions on hyperbolicity have been analyzed in Ref. [20].

It is worth noting that the speeds for some of the characteristic fields can exceed the speed of light. For example, the system E_{\pm}^{+} has a mode with speed $\sqrt{2/\alpha}$ that is superluminal for $\alpha < 2$, and a mode with speed $\sqrt{3/(\alpha^2\chi)}/2$ that is superluminal for $\alpha^2\chi < 3/4$. These modes are associated with the 1+log and Γ -driver gauge conditions [21]. As such, they appear in any formulation of the Einstein evolution equations that uses 1+log slicing and Γ -driver shift.

The constraint evolution system Eq. (11) is strongly hyperbolic with characteristic speeds 0, ± 1 . The respective characteristic fields are

$$\mathcal{H} + \chi\mathcal{G}^r, \quad (14a)$$

$$\mathcal{H} \mp 6\sqrt{\chi/g_{rr}}\mathcal{M}_r + 4\chi\mathcal{G}^{r'}. \quad (14b)$$

In three dimensions, the constraint propagation systems for both the GBSSN equations and the traditional BSSN

equations are strongly hyperbolic with causal characteristic speeds 0 and ± 1 .

V. BOUNDARY CONDITIONS

The one-dimensional code described in this paper could be used to evolve a single black hole with excision, or to evolve smooth spherically symmetric fields in \mathbb{R}^3 , provided appropriate boundary conditions are imposed. For the case of fields that are smooth at the origin, such as the fields that describe a spherically symmetric star, boundary conditions have been discussed in detail in Refs. [22, 23] and elsewhere. In this paper I will focus on boundary conditions that allow for black hole puncture evolution. In this case the origin $r = 0$ defines the puncture and is also a coordinate singularity in the underlying spherical coordinate system. The grid is cell centered with spacing Δr . The grid points are located at coordinate radii $r(j) = (j - 1/2)\Delta r$, where $j = 1, 2, \dots$

In applications involving smooth fields with spherical coordinates one would normally impose smoothness conditions at the origin [22, 23]. Specifically, scalars and type 2 tensors would be reflection symmetric and vectors would be antisymmetric. With puncture evolution we need to allow for the possibility that the fields will not remain smooth, even if they are smooth initially. We can nevertheless attempt to impose smoothness conditions at the puncture. In my experience this leads to an unstable code.

To obtain appropriate boundary conditions for puncture evolution I take a minimalist approach. That is, my goal is to impose as little information as possible through boundary conditions so that the puncture can evolve without unnecessary influence from the outside. After some experimentation, I found that the following prescription works well for the five Lagrangian cases L_0 and L_{\pm}^{\pm} . For the variables g_{rr} , χ , A_{rr} , K , Γ^r , α , and B^r , no boundary conditions are imposed. That is, for grid points near the puncture, the finite difference stencil is shifted away from the puncture so that no guard cells are needed.

Typically, the condition I impose on $g_{\theta\theta}$ and β^r is that these variables should vanish at the puncture. In keeping with the minimalist approach I only use one layer of guard cells. The guard cells ($j = 0$) are filled via the relations

$$g_{\theta\theta}(0) = [-315g_{\theta\theta}(1) + 210g_{\theta\theta}(2) - 126g_{\theta\theta}(3) + 45g_{\theta\theta}(4) - 7g_{\theta\theta}(5)]/63, \quad (15a)$$

$$\beta^r(0) = [-315\beta^r(1) + 210\beta^r(2) - 126\beta^r(3) + 45\beta^r(4) - 7\beta^r(5)]/63, \quad (15b)$$

where the numbers in parentheses denote grid points. These relations insure that $g_{\theta\theta}$ and β^r vanish at the puncture to sixth order accuracy. In other words, a fifth order polynomial fit across the grid points $j = 0 \dots 4$ with value (15) at $j = 0$ will yield a function that vanishes at $r = 0$.

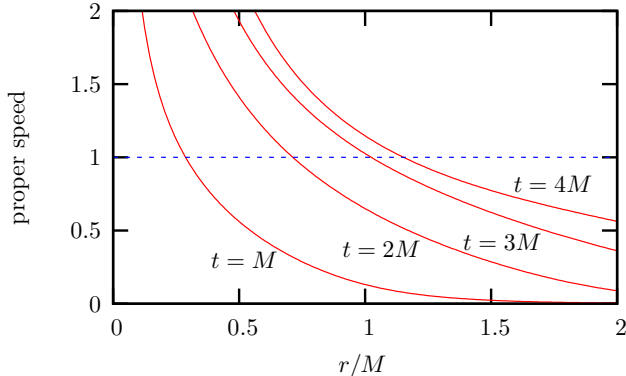


FIG. 1: The proper speed $\sqrt{(\beta^r)^2 g_{rr}}/\chi/\alpha$ of the coordinate system, plotted as a function of coordinate radius r at times $t = M, 2M, 3M$, and $4M$.

The results presented in Sec. VII are obtained from a code that uses fourth order accurate spatial differencing. In the bulk of the computational domain, I use centered stencils that extend across five grid points for first and second spatial derivatives. (An exception to this rule is made for advection terms like $\beta^r \partial_r g_{rr}$. For these terms, the finite difference stencil is shifted by one grid point in the “upwind” direction.) Since only one guard cell is available at the boundary $r = 0$, the stencils near $r = 0$ are shifted so that they require just one grid point on the side closest to the puncture.

For the Eulerian cases E_0 , E_+^+ and E_+^- , no boundary conditions are imposed on the variables g_{rr} , $g_{\theta\theta}$, χ , A_{rr} , K , Γ^r , α , and B^r . The only variable that remains is the shift vector β^r . For the shift I impose $\partial_r \beta^r = 0$ via the relationship

$$\beta^r(0) = [17\beta^r(1) + 9\beta^r(2) - 5\beta^r(3) + \beta^r(4)]/22. \quad (16)$$

Here again the numbers in parentheses label grid points. A fourth order polynomial fit across the grid points $j = 0 \dots 4$, with value (16) at $j = 0$, will yield a function with vanishing derivative at $r = 0$.

For the cases E_+^+ and E_+^- with the condition Eq. (16), an instability develops at the puncture within a time of a few M . I have not found suitable inner boundary conditions for these cases.

The minimalist approach to boundary conditions at $r = 0$ is not unreasonable. Simulations show that as the data evolve from the initial conditions, the light cones at grid points near the puncture quickly tip outward (toward $r = 0$) with respect to the time flow vector field. In Fig. (1) the proper speed of the coordinate system with respect to the spacelike slices is plotted at various times up to $t = 4M$. During the first $4M$ of evolution the horizon moves from $r = M/2$ to just beyond $r = M$. From the graph we see that by $t = M$ all of the grid points inside $r \approx M/3$ are moving faster than the speed of light

(which is unity). By $t = 4M$ the region of superluminal grid movement has expanded to about $r \approx M$, the location of the horizon. There is little change beyond $t = 4M$.

Once the time flow direction moves outside the light cone, one might expect that any boundary conditions imposed at the puncture would be irrelevant. This is not quite correct because GBSSN (as well as traditional BSSN) with 1+log slicing and Γ -driver shift contains characteristic modes that can travel faster than light. For example, the E_+^+ system has modes with speeds $\pm\sqrt{2/\alpha}$ and $\pm\sqrt{3/(4\alpha^2\chi)}$. The L_+^+ system has modes with speeds $\pm\sqrt{2/\alpha}$, $\pm\sqrt{1/(\alpha^2\chi)}$, and $\hat{\beta}^r$.

Ideally, one should impose boundary conditions on all incoming characteristic fields at the puncture. Whether or not a characteristic field is incoming or outgoing depends on the proper speed of the mode relative to the proper speed of the coordinate grid, which is $\hat{\beta}^r$. For a typical puncture evolution the modes listed in Eq. (13) with speeds $\pm\sqrt{2/\alpha}$ are outgoing, at least for times beyond the first few M . For E_+^+ , the characteristic field

$$\beta^{r'} - \frac{\sqrt{3g_{rr}}}{2} B^r + \frac{8\alpha\chi}{\sqrt{3g_{rr}}(8\alpha\chi - 3)} \alpha' + \frac{4\alpha}{8\alpha\chi - 3} K \quad (17)$$

has speed $\pm\sqrt{3/(4\alpha^2\chi)}$ and is incoming at the puncture throughout the evolution. Thus, we would expect that certain boundary information must be imposed at the puncture to fix this incoming mode. The condition Eq. (16) is not ideal, but appears to be sufficient to allow for stable evolutions. The case L_+^+ is more difficult to analyze, because in addition to an incoming mode it also contains a mode that travels along the puncture boundary.

The above discussion shows that for puncture evolution in one dimension, some boundary conditions at the puncture are necessary. This might come as a surprise since, apparently, no boundary conditions are imposed at the puncture in three-dimensional codes. This is probably an illusion. More likely, the incoming modes in the three-dimensional case are fixed implicitly through the numerical (finite differencing) scheme used in the vicinity of the puncture.

The details of the finite differencing scheme in the vicinity of the puncture would have little affect on the data away from the puncture, and would be especially difficult to detect outside the black hole. Evidence for this assertion can be found in recent work on the “turducken” approach to black hole evolution [14, 15, 24], in which the black hole interior is stuffed with artificial, constraint-violating data. In this case it is found, both for one-dimensional simulations with E_+^+ and for three-dimensional simulations with traditional BSSN, that the stuffing can only affect the slicing and coordinate conditions outside the black hole [15]. The slicing can be changed outside the black hole due to the presence of the mode Eq. (13) whose speed $\sqrt{2/\alpha}$ can become superluminal. However, inside a coordinate radius of about

$r \sim 0.2M$, this mode moves more slowly than the coordinate grid and cannot propagate to the black hole exterior. The coordinate conditions outside the black hole can be affected by the interior data through the presence of the mode Eq. (17). The conclusion is the following: the details of how the puncture is handled should not affect the spatial geometry or slicing of the black hole. Therefore, the boundary conditions at the puncture, whether they are imposed explicitly in one dimension or implicitly in three dimensions, do not affect the physics. Their only effect is to change the details of how the spatial coordinates are shifted in the spacelike slices.

Another subtle issue concerning the origin $r = 0$ is how the variable Γ^r is treated. Because Γ^r is singular at the puncture, $\Gamma^r \sim -2/r$, one would expect the finite difference calculation of $\Gamma^{r'}$ to generate large errors. This is indeed the case, but the errors are effectively trapped near the puncture. I have carried out numerical simulations using the “regularized” variable $\Gamma_{reg}^r \equiv \Gamma^r + 2/r$ in place of Γ^r ; a similar approach is advocated in Ref. [23]. In some cases this does help reduce the errors near the puncture, but it does not change the accuracy of the code elsewhere.

Finally, let me mention that at the outer boundary of the computational domain I use two layers of guard cells and simply freeze the data at those points. In general the outer boundary is placed at a coordinate distance that is greater than the total run time. Assuming causal propagation, the outer boundary conditions do not affect the fields near the puncture during the course of a simulation.

VI. KRUSKAL–SZEKERES DIAGRAM

One of the benefits of assuming spherical symmetry is that we can visualize the motion of the slices and grid points on a Kruskal–Szekeres diagram. In Kruskal–Szekeres coordinates, the Schwarzschild black hole metric is [25]

$$ds^2 = \frac{32M^3}{R} e^{-R/2M} (-dv^2 + du^2) + R^2 d\Omega^2 . \quad (18)$$

Each point in the u - v plane is a sphere of areal radius R , where R is defined by

$$u^2 - v^2 = \left(\frac{R}{2M} - 1 \right) e^{R/2M} . \quad (19)$$

Our goal is to track the numerical grid points as they move through the u - v plane.

There are a number of ways one can relate the numerical data to the u - v values of the grid points. I have had the most success with the following approach. Consider the metric for a spherically symmetric spacetime in 3+1 notation:

$$ds^2 = -(\alpha^2 - \beta^r \beta_r) dt^2 + 2\beta_r dt dr + \frac{g_{rr}}{\chi} dr^2 + \frac{g_{\theta\theta}}{\chi} d\Omega^2 . \quad (20)$$

Note that $\beta_r \equiv \beta^r g_{rr}/\chi$. Let $\mathcal{U} = \text{const}$ be a null curve in the r - t plane. By solving $d\mathcal{U} \equiv \partial_t \mathcal{U} dt + \partial_r \mathcal{U} dr = 0$ for dt and inserting the result into $ds^2 = 0$, we can easily show that \mathcal{U} satisfies $\hat{\partial}_\perp \mathcal{U} = \pm \hat{\partial}_r \mathcal{U}$. Here, the operator $\hat{\partial}_\perp \equiv (\partial_t - \beta^r \partial_r)/\alpha$ is the normalized derivative orthogonal to the spacelike hypersurface acting on scalars. The operator $\hat{\partial}_r \equiv \sqrt{\chi/g_{rr}} \partial_r$ is the normalized derivative tangent to the spacelike hypersurface. Now observe that $u \pm v$ are null coordinates. It follows that u and v satisfy the equations $\hat{\partial}_\perp(u+v) = \hat{\partial}_r(u+v)$ and $\hat{\partial}_\perp(u-v) = -\hat{\partial}_r(u-v)$, where the signs are chosen so that $\partial_r u$ is positive.

The reasoning above shows that the Kruskal–Szekeres coordinates satisfy the advection equations

$$\partial_t(u+v) = (\beta^r + \alpha \sqrt{\chi/g_{rr}}) \partial_r(u+v) , \quad (21a)$$

$$\partial_t(u-v) = (\beta^r - \alpha \sqrt{\chi/g_{rr}}) \partial_r(u-v) . \quad (21b)$$

We can integrate these equations forward in time along with the BSSN variables. To do so we must choose initial data and boundary conditions. The initial data for puncture evolution of a single black hole is obtained from the Schwarzschild metric in isotropic coordinates,

$$g_{rr} = 1 , \quad (22a)$$

$$g_{\theta\theta} = r^2 , \quad (22b)$$

$$\chi = (1 + M/2r)^{-4} , \quad (22c)$$

along with vanishing extrinsic curvature. The areal radius is $R \equiv \sqrt{g_{\theta\theta}/\chi} = r(1 + M/2r)^2$. If we assume that the initial slice is $v = 0$, Eq. (19) shows that $u = F(r)$ where $F(r)$ is defined by

$$F(r) \equiv \sqrt{\frac{r}{2M}} \left(1 - \frac{M}{2r} \right) e^{r(1+M/2r)^2/(4M)} . \quad (23)$$

More generally, we can take the initial slice to be boosted in the Kruskal–Szekeres diagram:

$$u = F(r) \cosh(t_0/4M) , \quad (24a)$$

$$v = F(r) \sinh(t_0/4M) . \quad (24b)$$

The constant t_0 represents the invariance of the Schwarzschild geometry under the action of the Killing vector field $v\partial_u + u\partial_v$. If we take $t_0 \neq 0$, then the initial data slice is related to $v = 0$ by sliding the slice along the orbits of the Killing vector field.

The freedom to choose t_0 is useful, because starting from $v = 0$ the slice quickly becomes stretched around the singularity $R = 0$. That is, on a Kruskal–Szekeres diagram, the slice becomes visually difficult to distinguish from the singularity after a few M of evolution time. We can avoid this somewhat by starting with an initial slice with $t_0 < 0$. In that case the early time slices are difficult to visualize, but the slices at times $t \approx t_0$ are clearly displayed in relation to the singularity and horizon. Another useful technique is to slide the slice along the Killing vector field after each timestep. This can be

used, for example, to keep grid points from crossing the v axis, or to fix the location in the Kruskal–Szekeres diagram where the slices cross the horizon.

The variables $u \pm v$ are left or right–moving, depending on the sign of $\beta^r \pm \alpha\sqrt{\chi/g_{rr}}$. For puncture evolutions, within a coordinate time of a few M , the shift vector grows and the lapse collapses so that β^r dominates over $\alpha\sqrt{\chi/g_{rr}}$ near $r = 0$. Therefore, beyond a time of a few M , both characteristic fields are outgoing (toward decreasing r) at the boundary $r = 0$. In the vicinity of the origin I use one–sided differencing for u and v , appropriate for outgoing fields. Thus, no guard cells are needed for u and v at $r = 0$.

At the outer boundary of the computational domain we have $\beta^r \approx 0$ and $\alpha\sqrt{\chi/g_{rr}} \approx 1$. Thus, the characteristic field $u + v$ is incoming and the field $u - v$ is outgoing. Boundary conditions are applied with the following scheme. First, let us equate the coefficients of dt^2 in Eqs. (18) and (20) to obtain

$$\dot{u}^2 - \dot{v}^2 = -\frac{R}{32M} e^{R/2M} (\alpha^2 - \beta^r \beta_r), \quad (25)$$

where the dot denotes ∂_t . Now differentiate the definition (19) with respect to time to obtain a second equation involving \dot{u} and \dot{v} . Together these equations have the solution

$$\dot{u} = \frac{1}{2G} \left(u\dot{G} + \varepsilon v \sqrt{\dot{G}^2 + 4GH(\alpha^2 - \beta^r \beta_r)} \right), \quad (26a)$$

$$\dot{v} = \frac{1}{2G} \left(v\dot{G} + \varepsilon u \sqrt{\dot{G}^2 + 4GH(\alpha^2 - \beta^r \beta_r)} \right), \quad (26b)$$

where $G \equiv (R/2M - 1) \exp(R/2M)$, $H \equiv (R/32M^3) \exp(R/2M)$, and $\varepsilon \equiv u/|u|$. Note that \dot{G} can be written in terms of R and \dot{R} . Also recall that the areal radius can be written in terms of the BSSN variables as $R = \sqrt{g_{\theta\theta}/\chi}$, so the time derivative \dot{R} depends on $\partial_t g_{\theta\theta}$ and $\partial_t \chi$. The time derivatives of these BSSN variables can be replaced with the right–hand sides of the BSSN equations (9a) and (9c).

Equations (26) are a set of ordinary differential equations for u and v . These can be integrated forward in time without the calculation of any spatial derivatives. I use these equations to determine u and v in the vicinity of the outer boundary, providing a layer of two guard cells for the interior calculation based on Eqs. (21a).

One can try to use Eqs. (26) to evolve u and v everywhere. In practice this does not work well. It is difficult to integrate these equations across the horizons where $G = 0$. Also it is difficult to maintain accuracy and stability as grid points evolve across the v axis, where the value of ε changes from -1 to $+1$.

Finally, let me mention a method for placing the data of a single time slice into a Kruskal–Szekeres diagram. From the numerical data one can compute the areal radius R and the proper distance from the horizon, L , for each grid point. In the u – v plane the metric gives

$$\Delta L^2 = \frac{32M^3}{R} e^{-R/2M} (\Delta u^2 - \Delta v^2). \quad (27)$$

We also find, by differentiating the definition (19),

$$u\Delta u - v\Delta v = \frac{R}{8M^2} e^{R/2M} \Delta R. \quad (28)$$

These equations can be solved for Δu and Δv as functions of ΔR and ΔL . The values of u and v for each grid point are found by numerical integration, starting from some initial values for u and v . These initial values must satisfy the restriction (19), which leaves some freedom of choice. For example, if the initial areal radius is less than $2M$, one can choose the initial values to be $u = 0$ and $v = \sqrt{1 - R/2M} e^{R/4M}$. The freedom in choosing the initial values for u and v is a consequence of the Killing isometry of Schwarzschild spacetime.

VII. RESULTS

There are a large number of cases that we can consider, depending on our choice of Eulerian versus Lagrangian evolution for g , the advection terms that we include or omit in the slicing and coordinate conditions, and the value for the damping parameter η that appears in the Γ –driver shift. I will not attempt to provide a complete examination and comparison of all these possibilities here. Rather, I will give a sampling of some of the interesting results.

The initial metric for puncture evolution is given in Eq. (22). Initially, the conformal connection function is $\Gamma^r = -2/r$, and the extrinsic curvature components A_{rr} and K vanish. The shift vector β^r and the auxiliary field B^r are chosen to vanish at the initial time. The initial lapse function is either unity, $\alpha = 1$, or has the “pre–collapsed” form $\alpha = (1 + M/2r)^{-2}$. In all cases the code uses fourth order finite differencing in space and fourth order Runge–Kutta for time stepping.

The geometrical description of puncture evolution for single black holes is now well understood [13, 21, 26, 27, 28]. The initial geometry is a wormhole. As the evolution begins, the grid points near the “other” asymptotically flat end quickly shift into the black hole interior. The numerical data then settle onto a portion of a “trumpet slice” of the black hole. Such a slice asymptotes to a constant areal radius of about $1.3M$. The key ingredient responsible for this behavior is the Γ –driver shift condition. Tests using the one–dimensional code with Γ –driver shift invariably show the same qualitative evolution for the physical geometry, the same evolution from wormhole to trumpet, for all of the cases E_{\pm}^{\pm} and L_{\pm}^{\pm} . However, the detailed behavior of the GBSSN variables can differ significantly from case to case.

Figures (2–5) show the metric components g_{rr} , $g_{\theta\theta}$, the conformal factor χ , and the shift vector β^r at time $t = 50M$ for the cases E_{+}^{\pm} and L_{+}^{\pm} . The data for these graphs were taken from simulations with resolution $\Delta r = M/100$. The differences near the puncture are evident.

One might guess that the difference between the cases E_{+}^{\pm} and L_{+}^{\pm} is a consequence of the different boundary

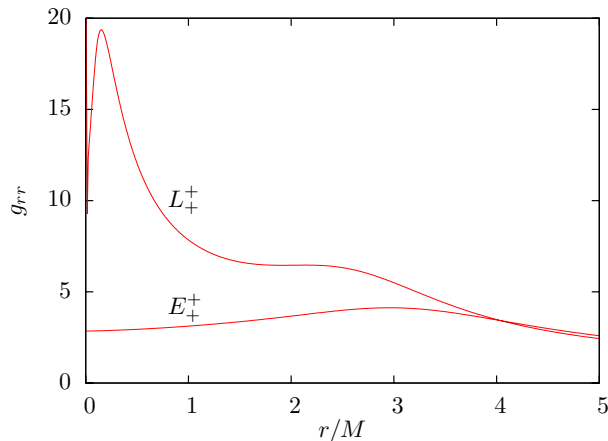


FIG. 2: The conformal metric component g_{rr} near the puncture $r = 0$ at time $t = 50M$ for the systems E_+^+ and L_+^+ .

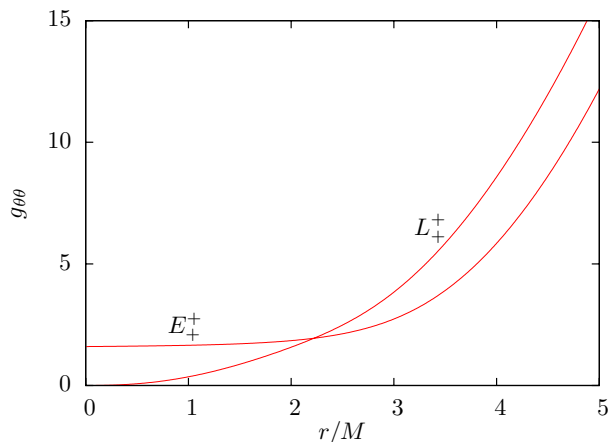


FIG. 3: The conformal metric component $g_{\theta\theta}$ at $t = 50M$ for E_+^+ and L_+^+ .

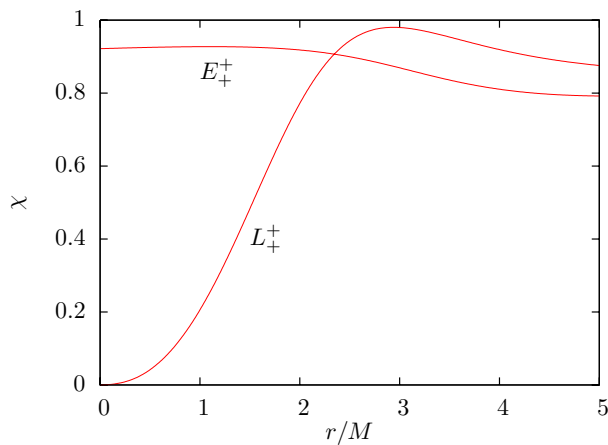


FIG. 4: The conformal factor χ at $t = 50M$ for E_+^+ and L_+^+ .

conditions imposed at $r = 0$. However, the Eulerian

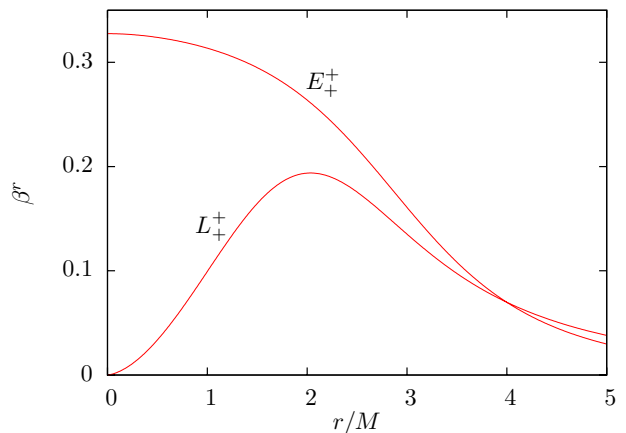


FIG. 5: The shift vector β^r at $t = 50M$ for E_+^+ and L_+^+ .

equations cannot be evolved with the Lagrangian boundary conditions (15). Recall that the Lagrangian boundary conditions are designed to keep $g_{\theta\theta}$ and β^r equal to zero at the puncture. If these conditions are used with the Eulerian evolution equations, the values of $g_{\theta\theta}$ and β^r near the puncture grow rapidly and a sharp gradient develops between the first few grid points $j = 1, 2, \dots$ and the guard cell $j = 0$. The code crashes shortly after $t = 1M$. With the boundary conditions (16), the fields $g_{\theta\theta}$ and β^r are allowed to develop nonzero values at the puncture. Figures (3) and (5) show that indeed $g_{\theta\theta}$ and β^r evolve to nonzero values in the Eulerian case E_+^+ .

The converse is also true: The Lagrangian equations will not evolve stably with the Eulerian boundary conditions (16). If one attempts such an evolution, the code quickly develops problems at the puncture and crashes. It appears that the behavior of the fields near the puncture is primarily dictated by the equations of motion in the bulk. Perhaps the main role played by the boundary conditions (15) or (16) is to help insure numerical stability for the GBSSN equations in spherical symmetry.

Although the results obtained with E_+^+ and L_+^+ appear quite different, they represent the same slicing of the same spacetime geometry. It is clear that the spacetime geometry is that of a Schwarzschild black hole, since a Schwarzschild black hole is the unique solution of the vacuum Einstein equations with the chosen initial data. It is not quite so obvious that the evolutions E_+^+ and L_+^+ lead to the same foliation of that spacetime geometry. The difference between the Eulerian and Lagrangian cases resides in the choice for $\partial_\perp \ln g$, as seen in Eqs. (5). The terms containing $\partial_\perp \ln g$ can be absorbed into redefinitions of the field variables. For example, Eq. (5a) can be written as $\partial_\perp \hat{\phi} = -\alpha K/6$ where $\hat{\phi} \equiv \phi + \ln g^{1/12}$. Similarly, Eq. (5b) can be written as $\partial_\perp \hat{g}_{ab} = -2\alpha A_{ab}$ where $\hat{g}_{ab} \equiv g^{-1/3} g_{ab}$. The physical metric (3a) is invariant under this redefinition: $e^{4\hat{\phi}} \hat{g}_{ab} = e^{4\phi} g_{ab}$. This invariance is a consequence of the conformal symmetry of the GBSSN equations [16]. In this way we see that, independent of

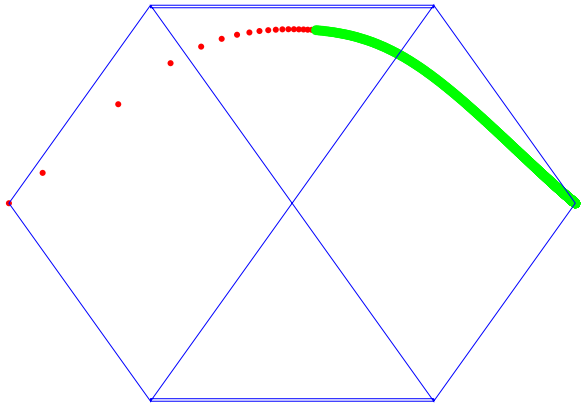


FIG. 6: Penrose diagram showing the grid points for the cases E_+^+ (large green circles) and L_+^+ (small red circles) at time $t = 2.5M$. The data for E_+^+ blend together to form a thick curve that ends in the middle of the diagram.

the choice for $\partial_\perp \ln g$, the physical metric and extrinsic curvature undergo identical evolutionary paths.

Figure (6) shows a penrose diagram with the grid points at time $t = 2.5M$ as obtained from the E_+^+ and L_+^+ cases. The slice is the same for the two cases. What is clearly different is the coverage of that slice by the available grid points. In the Eulerian case, the relatively large positive shift near the puncture, seen in Fig. (5), drives the grid points away from the left spacelike infinity and into the interior of the black hole. In the Lagrangian case the grid points are also driven from the left spacelike infinity into the black hole interior, but not as quickly.

The behavior of the three-dimensional GBSSN equations in the case L_+^+ appears to be close to the behavior of three-dimensional BSSN codes. It is particularly useful to compare the results presented below with those of Ref. [7]. In particular, Figs. (7–10) show graphs of the variables g_{rr} , χ , α , and β^r as functions of the coordinate radius r at time $t = 50M$. The evolution is type L_+^+ (Lagrangian case with 1+log slicing including the advection term and Γ -driver shift excluding advection terms), and begun with a pre-collapsed lapse. The resolution used for these simulations was $\Delta r = M/100$. The curves in these figures show the results obtained with three values of the damping parameter, $\eta = 0$, $\eta = 1/M$, and $\eta = 2/M$.

Recall that η appears in the Γ -driver shift condition. For 1+log slicing including the advection term the shift vector does not affect the slicing of spacetime or the spatial geometry, it only changes the coordinate system (or distribution of grid points) from one slice to the next [13]. Thus the results obtained with different values of η are physically equivalent. Nevertheless, there is reason to prefer a value that will allow the lapse and shift to adjust to the Killing symmetry of the Schwarzschild geometry. That is, we want the gauge to be “symmetry

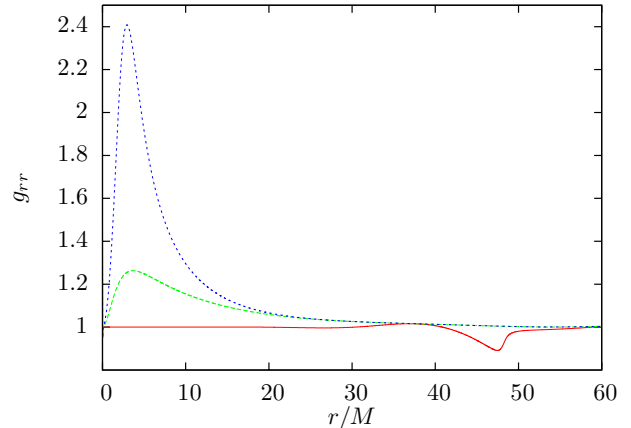


FIG. 7: g_{rr} as a function of coordinate radius r at time $t = 50M$ for the case L_+^+ . The three curves correspond to values 0, $1/M$, and $2/M$ for the damping parameter η . The peak values increase with increasing η .

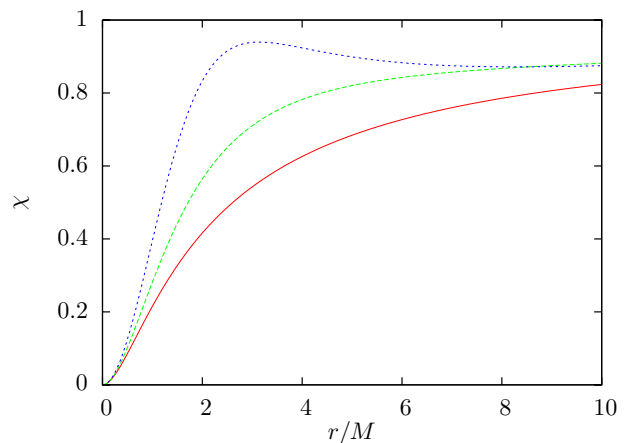


FIG. 8: χ as a function of r at time $t = 50M$ for the case L_+^+ with $\eta = 0$, $1/M$, and $2/M$. The peak values increase with increasing η .

seeking” and bring the data close to a stationary state at late times [21]. For the one-dimensional code with 1+log slicing the value $\eta = 0$ is a good choice. With $\eta = 0$ the data settle very close to a stationary state by $t = 50M$.

With positive η the data continue to evolve indefinitely. This tendency has been seen in three-dimensional simulations [7] where it is described as “coordinate drift”. We can monitor this drift by computing the L2 norm of the right-hand sides of the GBSSN equations. (The L2 norm is defined as a sum over the right-hand sides of the evolution equations for g_{rr} , χ , K , Γ^r , α , and β^r , and a sum over grid points between $r = 0$ and $r = 25M$.) For each value of η the L2 norm rises to a peak value just beyond $t = 2M$. For $\eta = 0$ the norm drops slowly between $t \approx 2M$ and $t \approx 25$, then drops rapidly for $t > 25M$. The sudden change in slope at $t \approx 25M$ occurs for the following reason. At early times there is a relatively large

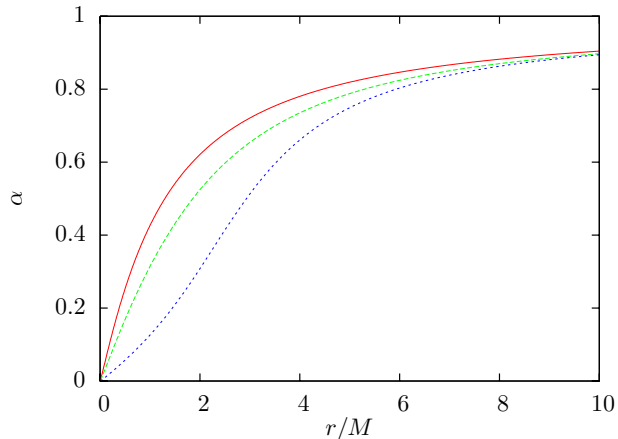


FIG. 9: α as a function of r at time $t = 50M$ for the case L_-^+ with $\eta = 0, 1/M,$ and $2/M$. The peak values decrease with increasing η .

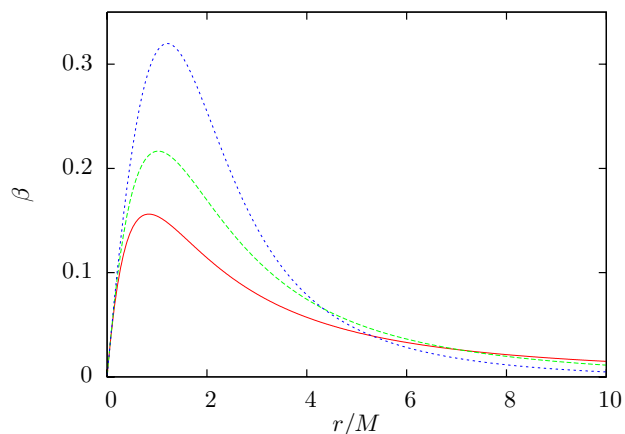


FIG. 10: β^r as a function of r at time $t = 50M$ for the case L_-^+ with $\eta = 0, 1/M,$ and $2/M$. The peak values increase with increasing η .

adjustment in the geometry near the puncture as the grid points near the puncture pull away from spacelike infinity, enter the black hole interior, and relax to the “trumpet slice” [13]. This adjustment can be seen in the values of the right-hand sides as a pulse that propagates outward. At $t \approx 25M$ the pulse passes beyond the region in which the L2 norm is computed. The rapid decay for $\eta = 0$ beyond $t \approx 25M$ shows that the data in the interior region $r < 25M$ of the computational grid is very effectively becoming stationary.

The code described here uses fourth order finite differencing in space and time. However, the code does not always exhibit fourth order convergence near the puncture. Figures (12) and (13) show convergence plots for χ at early and late times, $t = 2M$ and $t = 50M$, for the case L_-^+ . Each graph shows three curves, obtained by computing differences between values of χ at successive resolutions and scaling by powers of 16. To be explicit, let

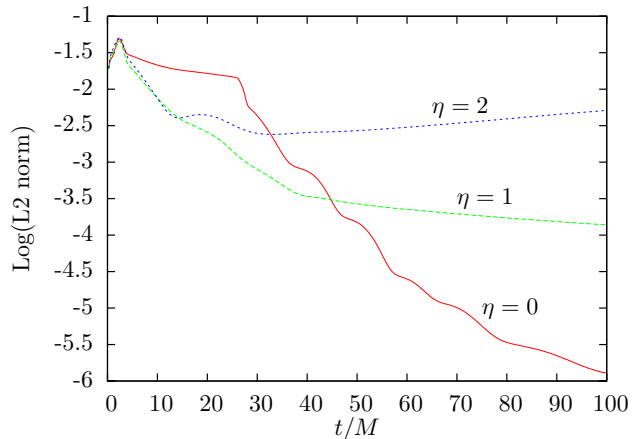


FIG. 11: Common Logarithm of the L2 norm of the right-hand sides of the equations of motion versus time.

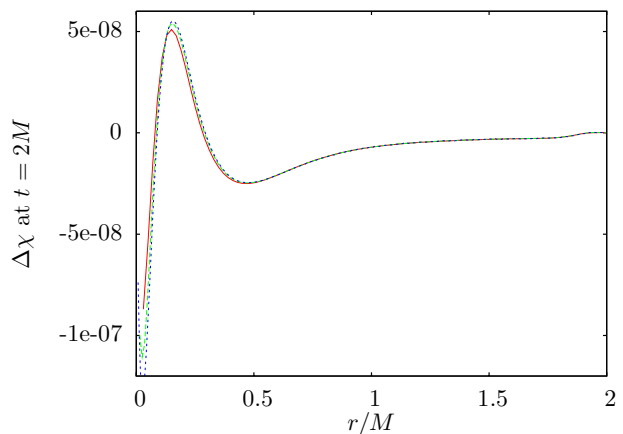


FIG. 12: Convergence plot for χ at $t = 2M$. The data are obtained from simulations at resolutions $\Delta r = M/50, M/100, M/200,$ and $M/400$. The curves are scaled by powers of 16, appropriate for fourth-order convergence.

us add a subscript to χ to denote the resolution Δr . Then the curves in Figs. (12) and (13) are $(\chi_{M/50} - \chi_{M/100}), 16(\chi_{M/100} - \chi_{M/200}),$ and $256(\chi_{M/200} - \chi_{M/400})$. These graphs show that at early times the data are fourth-order convergent, while at late times the data are fourth order convergent outside the region close to the puncture.

Figure (14) is a convergence plot for χ at the intermediate time $t = 15M$, again for the system L_-^+ . This graph shows four curves, $(\chi_{M/50} - \chi_{M/100}), 4(\chi_{M/100} - \chi_{M/200}), 16(\chi_{M/200} - \chi_{M/400}),$ and $64(\chi_{M/400} - \chi_{M/800})$. The curves are scaled by powers of 4, which is the scaling expected for second-order convergence. An error pulse is generated near the puncture and propagates outward through the computational domain. Note that this error is delayed at higher resolution, resulting in a shift in the curves.

These tests suggest that the puncture generates an ap-

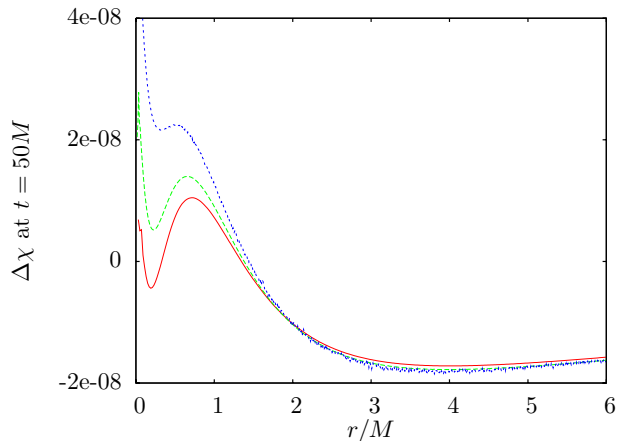


FIG. 13: Convergence plots for χ at $t = 50M$. The resolutions and scaling are the same as those used in Fig. (12).

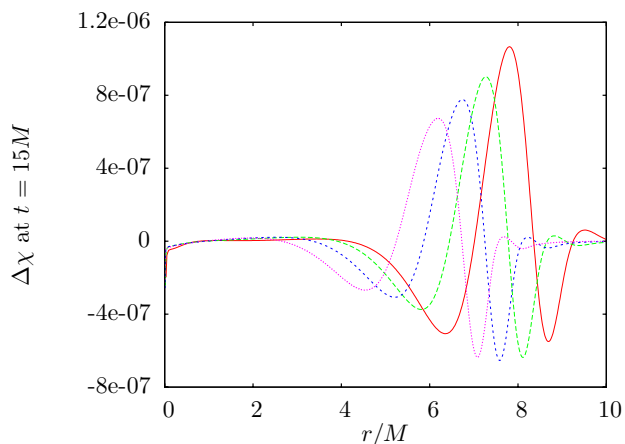


FIG. 14: Convergence plot for χ at $t = 15M$. The resolutions are the same as those used in the previous figures. In this case the curves are scaled by powers of 4, appropriate for second-order convergence.

proximately second-order error of the form

$$\chi_{\Delta r} = \chi_{\text{exact}} + \frac{\Delta r^2}{r} \mathcal{E}(r - t + 2M \log(M/\Delta r)) \quad (29)$$

for some function \mathcal{E} . The pulse appears to form from errors near the puncture. Note that the horizon begins at coordinate radius $r = M/2$ and stays within $r \leq M$ throughout the evolution. The pulse moves with a speed of approximately 1. It has an amplitude approximately proportional to $\Delta r^2/r$. At higher resolution the pulse is delayed. This delay appears as a shift toward the puncture in Fig. (14). The amount of delay or shift is proportional to the logarithm of $1/\Delta r$.

Similar convergence tests with the E_+^+ system do not show this anomalous behavior. This suggests that the origin of the non-fourth order error for L_-^+ is related to the presence of modes with the unusual proper speed $\hat{\beta}^r$.

Because the characteristic fields and speed for traditional BSSN are more closely related to those for E_+^+ , I would not expect to see such behavior in current 3D codes using the traditional BSSN equations.

Figure (15) shows a plot of the L2 norm of the constraints (10) as functions of time. The constraint values are stable over time, with only the Hamiltonian constraint \mathcal{H} showing a slight upward drift. All of the constraints exhibit large non-convergent errors near the puncture. These errors dominate the calculation of the L2 norm over the entire computational domain. As a result, the data for Fig. (15) was obtained by omitting the region $0 < r < 0.5M$. The data beyond $r > 25M$ is also excluded so that outer boundary effects are ignored. The data for the momentum constraint \mathcal{M}_r and the conformal connection function constraint \mathcal{G}^r show nearly perfect fourth order convergence over this region $M/2 < r < 25M$. The results for the Hamiltonian constraint \mathcal{H} are not so ideal. I suspect this is related to errors that arise in computing \mathcal{H} , which depends on second spatial derivatives of the metric components $g_{\theta\theta}$ and χ . The constraints \mathcal{M}_r and \mathcal{G}^r do not involve second order derivatives.

The flow of grid points on a Kruskal–Szekeres diagram can be particularly enlightening. Figure (16) shows the grid points at $t = 50M$ located on a portion of the Kruskal–Szekeres diagram. This data was obtained from a simulation L_-^+ with $\eta = 0$, and initial lapse $\alpha = 1$. The initial slice in the diagram was obtained from Eq. (24) with $t_0 = -50M$. The resolution for this simulation was $\Delta r = M/100$. For clarity, only the odd numbered grid points are shown in this figure. The smooth curve was obtained from a simulation with vanishing shift vector, case L_0 .

The first grid point in Fig. (16), $j = 1$, is at location $u \approx -3.7$, $v \approx 3.7$ between the horizon and the physical

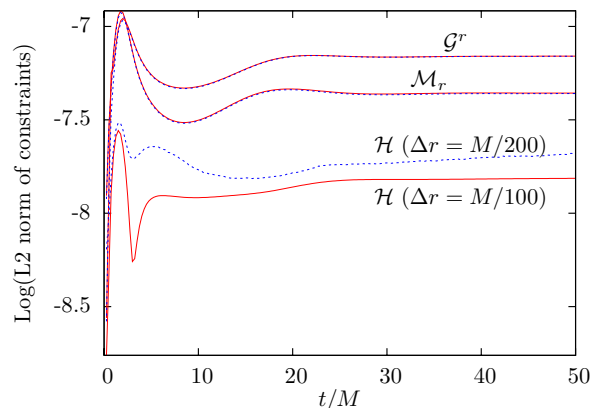


FIG. 15: Common log of the L2 norm of the constraints \mathcal{H} , \mathcal{M}_r , and \mathcal{G}^r . For each constraint two resolutions are plotted, $\Delta r = M/100$ and $\Delta r = M/200$. For the higher resolution, the constraints are multiplied by a factor of 16. The two curves for \mathcal{M}_r overlap one another, and are nearly indistinguishable in this figure. Likewise the two curves for \mathcal{G}^r overlap one another.

singularity. As shown in Ref. [13], the grid points near the puncture are rapidly drawn into the black hole interior by the Γ -driver shift condition. This is, however, a resolution-dependent effect. In the limit of infinitely high resolution, the grid points merge into the smooth curve. That curve crosses the horizon and asymptotes to spacelike infinity ($u \sim -\infty, v \sim \text{finite}$).

Figure (17) compares the results of simulations with cases L^- and L_0 . Again, we use $\eta = 0$, unit initial lapse, and choose $t_0 = -50M$. The figure shows grid points $j = 3, 5, 7 \dots$ at time $t = 50M$ for the L^- evolution. The grid point $j = 1$, which is not shown, is at location $u \approx -12.7, v \approx 12.7$. The smooth curve on the Kruskal-Szekeres diagram was obtained from the L_0 evolution. Note that in this case the grid points do not lie on the curve. This is because without the advection term in the 1+log slicing condition, the slicing depends on the shift vector.

Finally, let me comment on the results of long term evolution. Typically, after a run time on the order of a few light crossing times, the code will crash due to the development of a shock. For example, with E_+^+ evolution on a grid with outer boundary at $125M$, steep gradients and spikes develop in the BSSN variables at about $r \approx 8.5M$. The behavior causes the code to crash at $t \approx 250M$. With the outer boundary placed at $75M$, the shock develops at $r \approx 6M$ and the code crashes at $t \approx 160M$. It is possible that improvements to the outer boundary conditions might postpone or even eliminate

these shocks. On the other hand, it has been suggested that gauge shocks are a generic result of 1+log type slicing conditions [21]. Currently, such behavior has only been seen with 1+1 codes.

Acknowledgments

I would like to thank Dae-Il Choi, Pablo Laguna, Olivier Sarbach and Manuel Tiglio for helpful discussions. This work was supported by NSF grant PHY-0600402.

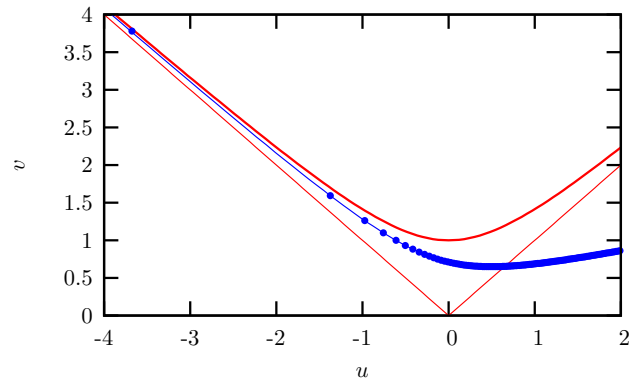


FIG. 16: Kruskal diagram at $t = 50M$ for simulations with 1+log slicing. The hyperbolic curve is the future singularity and the lines at $\pm 45^\circ$ are the horizons.

-
- [1] M. Shibata and T. Nakamura, Phys. Rev. **D52**, 5428 (1995).
 - [2] T. W. Baumgarte and S. L. Shapiro, Phys. Rev. **D59**, 024007 (1999), gr-qc/9810065.
 - [3] M. Campanelli, C. O. Lousto, P. Marronetti, and Y. Zlochower, Phys. Rev. Lett. **96**, 111101 (2006), gr-qc/0511048.
 - [4] J. G. Baker, J. Centrella, D.-I. Choi, M. Koppitz, and J. van Meter, Phys. Rev. Lett. **96**, 111102 (2006), gr-qc/0511103.
 - [5] F. Herrmann, D. Shoemaker, and P. Laguna (2006), gr-qc/0601026.
 - [6] U. Sperhake (2006), gr-qc/0606079.
 - [7] B. Brugmann, J. González, M. Hannam, S. Husa, and U. Sperhake, Phys. Rev. **D77**, 024027 (2008), gr-qc/0610128.
 - [8] J. A. Gonzalez, U. Sperhake, B. Bruegmann, M. Hannam, and S. Husa, Phys. Rev. Lett. **98**, 091101 (2007), gr-qc/0610154.
 - [9] M. Campanelli, C. O. Lousto, Y. Zlochower, B. Krishnan, and D. Merritt, Phys. Rev. **D75**, 064030 (2007), gr-qc/0612076.
 - [10] J. G. Baker, S. T. McWilliams, J. R. van Meter, J. Centrella, D.-I. Choi, B. J. Kelly, and M. Koppitz (2006), gr-qc/0612117.
 - [11] J. Thornburg, P. Diener, D. Pollney, L. Rezzolla, E. Schnetter, E. Seidel, and R. Takahashi (2007), gr-qc/0701038.

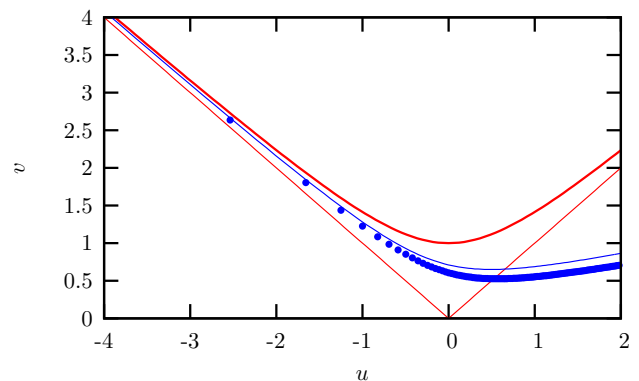


FIG. 17: Kruskal-Szekeres diagram at $t = 50M$ for simulations with slicing condition $\partial_t \alpha = -2\alpha K$.

- [12] W. Tichy and P. Marronetti (2007), gr-qc/0703075.
- [13] J. D. Brown (2007), arXiv:0705.1359 [gr-qc].
- [14] J. D. Brown, O. Sarbach, E. Schnetter, M. Tiglio, P. Diener, I. Hawke, and D. Pollney, Phys. Rev. **D76**, 081503 (2007), arXiv:0707.3101 [gr-qc].
- [15] J.D. Brown, P. Diener, O. Sarbach, E. Schnetter, and M. Tiglio, in progress.
- [16] J. D. Brown, Phys. Rev. **D71**, 104011 (2005), gr-qc/0501092.
- [17] J. R. van Meter, J. G. Baker, M. Koppitz, and D.-I. Choi,

- Phys. Rev. **D73**, 124011 (2006), gr-qc/0605030.
- [18] G. Nagy, O. E. Ortiz, and O. A. Reula, Phys. Rev. **D70**, 044012 (2004), gr-qc/0402123.
- [19] H. Beyer and O. Sarbach, Phys. Rev. **D70**, 104004 (2004), gr-qc/0406003.
- [20] C. Gundlach and J. M. Martin-Garcia, Phys. Rev. **D74**, 024016 (2006), gr-qc/0604035.
- [21] D. Garfinkle, C. Gundlach, and D. Hilditch (2007), arXiv:0707.0726 [gr-qc].
- [22] M. Alcubierre and J. A. Gonzalez, Comput. Phys. Commun. **167**, 76 (2005), gr-qc/0401113.
- [23] M. Ruiz, M. Alcubierre, and D. Nunez, Gen. Rel. Grav. **40**, 159 (2008), 0706.0923.
- [24] Z. B. Etienne, J. A. Faber, Y. T. Liu, S. L. Shapiro, and T. W. Baumgarte, Phys. Rev. **D76**, 101503 (2007), 0707.2083.
- [25] C. W. Misner, K. S. Thorne, and J. A. Wheeler, *Gravitation* (Freeman, 1973).
- [26] M. Hannam, S. Husa, D. Pollney, B. Brügmann, and N. O’Murchadha (2006), gr-qc/0606099.
- [27] M. Hannam, S. Husa, B. Brügmann, J. González, U. Sperhake, and N. O’Murchadha (2006), gr-qc/0612097.
- [28] M. Hannam, S. Husa, F. Ohme, B. Brugmann, and N. O’Murchadha (2008), 0804.0628.